Comparison of Alternative Floater concepts for a 2-span Suspension Bridge supported by a Tension Leg Platform

Mitja Papinutti, Jörg Sello

Bentley Systems Austria, Graz, Austria

Arne Bruer, Mathias Marley

TDA COWI AS, Oslo, Norway

Johannes Veie, Simen Hellgren Holtberget

Norwegian Public Roads Administration, Oslo, Norway

Contact: Mitja.Papinutti@Bentley.com

Abstract

As part of the E39 fjord crossing project The Norwegian Public Roads Administration (NPRA) performs a feasibility study of crossing the 2000m wide and 500m deep Halsafjord with a fixed link. One possible crossing alternative is a two span suspension bridge supported by a Tension Leg Platform (TLP) mid-fjord. The TLP technology is adopted from the offshore industry where it has been proven to be an effective concept for floating constructions at large water depths. Two floater concepts, a 4-legged steel floater and a monoleg concrete floater with a large submerged disk, are considered. The two floater concepts have similar stiffness properties, but large difference in inertia and shape. The structural response in a severe storm is calculated for the bridge subject to wind, wave and current forces, comparing the motion behaviour of the two floater concepts. Analyses are performed in time domain in software package RM Bridge, taking hydrodynamic, hydrostatic and aerodynamic load effects into account.

Keywords: floating bridge, suspension bridge, hydrodynamics, wave loading, aerodynamics, wind buffeting, time domain analysis.

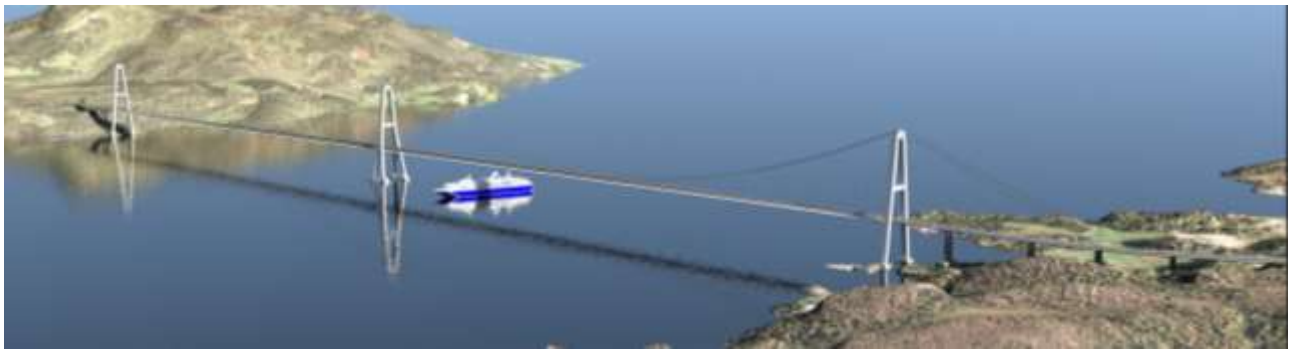

Figure 1. Overview of the bridge, shown with the 4-legged steel floater concept. Courtesy Arne Jørgen Myhre, Norwegian Public Road Administration.

1 Introduction

1.1 Project background

The Norwegian Public Roads Administration (NPRA) is currently working on the ferry free E39 project. The project goal is to connect Kristiansand in the south of Norway with Trondheim in the middle of Norway with a continuous stretch of road. The route spans along the west coast of Norway, and is approximately 1100 kilometres long. There are several fjords along the west coast of Norway, eight of which have to be crossed in order to build the whole stretch of road. One of the crossings, Rogfast just north of Stavanger, will be a record-breaking subsea rock tunnel, where the construction works are planned to start in 2018. It is planned to cross the remaining seven fjords with a fixed link. The fjords are both wide and deep, and introduce some new challenges when it comes to bridge design. As traditional bridge or subsea tunnel designs are not applicable for the longest and deepest crossings, new bridge concepts need to be developed. Among several proposed concepts, the NPRA has selected three main concepts for further investigations: One concept is a floating pontoon bridge, constructed as a straight side anchored bridge, or as a curved end anchored "bucket handle" type. The second concept is a submerged floating tube bridge, anchored by tendons or floated by pontoons. The third concept is a multi-span suspension bridge supported by floating foundations. The NPRA is currently working on developing these concepts in cooperation with the universities and the consultancy industry in Norway.

1.2 Description of floater concepts

This project is a feasibility study on a new bridge concept [1] for crossing the 2000m wide and 500m deep Halsafjord. The bridge concept, shown in Figure 1, consists of a 2-span suspension bridge, supported by a tension leg platform in the middle of the fjord and two fixed traditional concrete pylons onshore.

Due to uncertain seabed conditions, the bridge considered in this study has two main spans of 1200m length, providing flexibility in placement of the floating foundation. The water depth is approximately 500m at the chosen floater position.

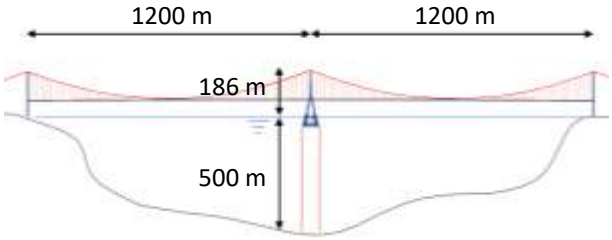

Figure 2. Overview of the bridge geometry.

The tension leg platform (TLP) concept is used by the offshore industry to provide a stable working platform at large water depths. The tension legs (tendons) provide large stiffness in the vertical direction as well as for rotation about the two horizontal axes. The horizontal stiffness of the floater, $k_{x,z}$, is provided by the total tension in the tendons as

$$k_{x,z} = \frac{\text{buoyancy} - \text{weight}}{\text{tendon length}}, \qquad (1)$$

where *buoyancy* is the net hydrostatic pressure acting on the floater and *weight* is the total weight supported by the floater. The coordinate system used has x in the longitudinal bridge direction, z in the lateral bridge direction and y vertically upwards.

In addition there is significant stiffness offered by the superstructure in both horizontal directions. The geometric stiffness of the superstructure from a point load in the lateral direction at the floater can be calculated from the total pre-tensioning in the main cables as

$$k_z = \frac{\text{total horizontal cable force}}{\text{span length}}. \qquad (2)$$

1.3 Description of floater concepts

Two floater concepts are considered in the present study, which differ both in displacement and shape; a lightweight 4-legged steel hull (depicted in Figure 3) similar in shape to many traditional offshore platforms, and a monoleg concrete hull (depicted in Figure 4) with a large submerged disk providing buoyancy. Both concepts are given

similar tendon stiffness properties in all degrees of freedom. The total tendon tension is set to 200MN. This is likely to be updated once further investigations into tendon capacity towards slack and dynamic loading are performed.

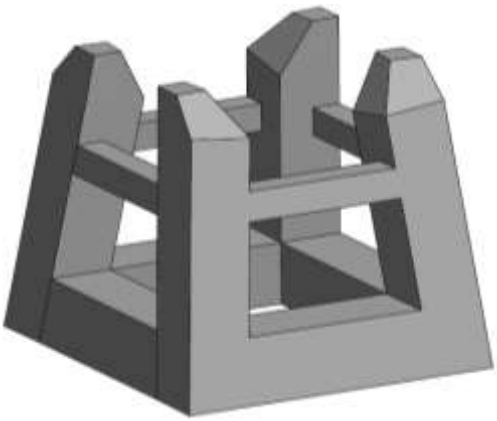

Figure 3. The 4-legged steel hull has a displacement of 77 000m3. The concept consists of 4 tilted square legs with 13.5x13.5m cross section, transitioning into 6x6m cross section above sea level. The draft is 52m at mean sea level.

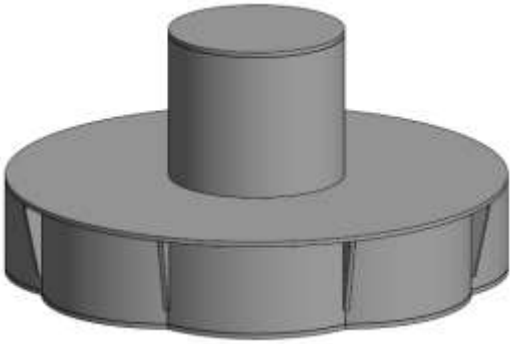

Figure 4. The monoleg concrete hull has a displacement of 207 000m3. The lower disk has an outer diameter of 100m and height of 20m. The surface piercing cylinder has a diameter of 35m and height of 30m. The hull extends 10m above mean sea level, giving it a design draft of 40m.

2 Analysis Model

2.1 Structural model

A structural model of the bridge, depicted in Figure 5, is developed in RM Bridge [2], using 12 Degrees Of Freedom (DOF) line elements for pylons and bridge deck, and cable elements for cables and hangers. The connection between the deck and the abutments is simulated with nonlinear viscous damper elements.

The submerged parts of the floaters are modelled as rigid bodies connected to the seabed by massless cable elements representing the tendons. The rigid body assumption is necessary for including hydrodynamic properties and is sufficient for global response analysis as well as analysis of the superstructure and tendons. The two models differ only in floater and tendon configuration.

Figure 5. Overview of RM Bridge Analysis model with the 4-legged steel floater concept.

2.2 Dynamic equation of motion

For time integration a classical trapezoidal Newmark integration scheme is used. The dynamic equation of motion is assembled as

$$M \cdot \ddot{x} + C \cdot \dot{x} + K \cdot x = \mathrm{F}, \qquad (3)$$

where M is mass matrix of structure, C is Rayleigh damping, K is nonlinear tangent stiffness and F is external forces. The water-structure interaction and wind-structure interaction are calculated inside the nonlinear Newmark integration step. The numerical integration is an implicit-explicit scheme. The constant matrices are solved with implicit approach on the left side of the equation, while nonlinear terms are placed on the right side and solved iteratively for dynamic equilibrium. Fluid-structure interactions are represented by additional matrices to the global structural matrices of the bridge, and includes added mass, added damping and added stiffness. Analysis are performed fully coupled considering all interaction, loads and nonlinear structural properties. Iteration is used for the dynamic equilibrium to be reached inside the nonlinear Newmark time step [3]. The dynamic equilibrium considering all interactions and loads can be rewritten as

$$\begin{aligned}&\left(\mathrm{M}+M_{HY}(\omega)\right)\cdot\ddot{x}+\\&(C+C_{HY}(\omega)+C_{AE})\cdot\dot{x}+C_V\cdot\dot{x}^2\\&(K+K_{HY}+K_{AE})\cdot x=F_{wave}+F_{wind},\end{aligned}\qquad(4)$$

where K_{HY} is hydrostatic stiffness, C_V is hydrodynamic viscous damping, C_{AE}, K_{AE} are aerodynamic damping and stiffness, F_{wave}, F_{wind} are time dependet wind and wave loads. $M_{HY}(\omega)$, $C_{HY}(\omega)$ are the frequency dependent added mass and damping terms, which need to be given special treatment in time domain. In following chapters mathematical formulation of water structure interaction is described, for bridge and surrounding sea, and wind-bridge interaction, for bridge under wind buffeting load.

The bridge response is considering a fully nonlinear geometrical analysis with large displacement theory, cable nonlinear analysis, nonlinear damper analysis and fully coupled nonlinear interaction of wind and waves.

3 Water-Structure interaction

3.1 Hydrostatic properties

Hydrostatic buoyancy force is applied as a structurally fixed vertical force positioned in the center of buoyancy. This ensures that the destabilizing moment of the buoyancy force for rotations about the horizontal axes is included in the analysis. The hydrostatic restoring forces due to change in displaced volume of the submerged hull (waterplane stiffness) are modelled as linear springs,

$$K_{HY}=[0\quad k_y\quad 0\quad k_{rx}\quad k_{rz}\quad 0\ ]\qquad(5)$$

where k_y is the stiffness coefficient for vertical displacement, k_{rx} and k_{ry} are the stiffness coefficients for rotation about x-axis and z-axis respectively.

3.2 Hydrodynamic radiation forces

The hydrodynamic properties of the hull, shown in Figure 6 for the lateral direction, are obtained from a potential theory analysis using the Ansys AQWA software package [5]. The hydrodynamic added mass is written as a constant term and a frequency-dependent term,

$$M_{HY}(\omega)=M_{hy}(\omega)+M_{HY}(\omega=\infty)\qquad(6)$$

where $M_{HY}(\omega=\infty)$ is added mass at infinite frequency and $M_{hy}(\omega)$ is the frequency-dependent variation about this.

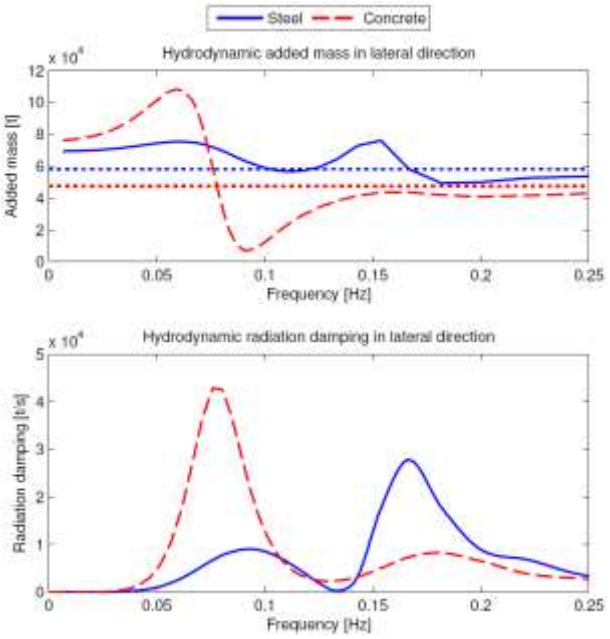

Figure 6. Added mass (top) and radiation damping (bottom) in the lateral direction. Dotted lines is the added mass at infinity frequency.

The frequency-dependent terms can, according to Cummins [4], be included in time domain as a hydrodynamic radiation force $\mathrm{C}(t)$. This requires a convolution integral,

$$C(t)=\int_0^t R(t-\tau)\dot{x}(\tau)d\tau,\qquad(7)$$

were

$$R(t)=\frac{2}{\pi}\int_0^\infty C_{HY}(\omega)\cos(\omega t)d\omega\qquad(8)$$

is the retardation function of the hydrodynamic radiation force. $C(t)$ is a function of the motion history of the floater, and includes both inertial forces and dissipative forces.

3.3 Hydrodynamic viscous forces

Nonlinear hydrodynamic viscous drag and damping is modelled as

$$F_d = \frac{1}{2}\rho C_d D(U_{elem.} - U_{curr})^2, \quad (9)$$

where F_d is integrated along the structural element to obtain the viscous force. C_d is the drag coefficient, D is the diameter, U_{elem} is the element velocity and U_{curr} is the current velocity.

3.4 Wave excitation

For TLP-structures in moderate sea states the wave excitation can be considered uncoupled from the motion of the body. This allows us to model the wave loads as force time histories calculated externally prior to simulation.

First order wave loads are included in the present study. The wave excitation is generated using transfer functions providing the relation between incoming waves and structural load. The incoming waves are modelled as a stochastic process from wave spectra believed to be representative of the Halsafjorden. Locally wind-generated waves and ocean swell is modelled as separate wave trains, with linear superposition of the wave excitation. The wave excitation spectra due to the sea states given in Table 1 are provided in Figure 7. The large difference in excitation is due to hull geometry.

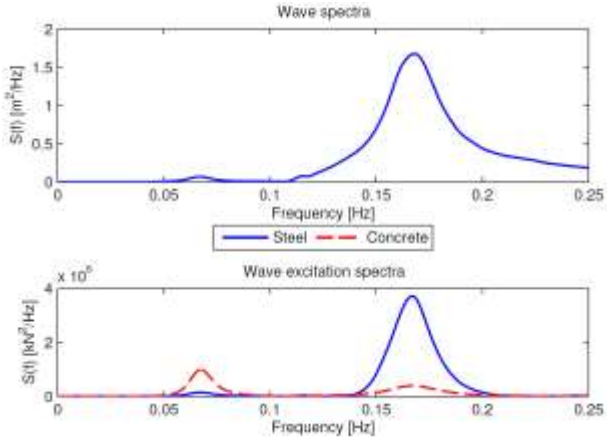

Figure 7. Wave spectra and wave excitation for the lateral direction from combined wind sea and ocean swell.

3.5 Metocean conditions

Reliable environmental data for Halsafjorden is not yet available. The chosen meatocean conditions, shown in Table 1, are believed to be representative of a 1 year return period storm. This can be considered as a serviceability limit state, where safe operation of the bridge is a requirement. Wind sea, ocean swell and current are assumed propagating in the same direction transversal to the bridge.

Table 1. Metocean conditions

Load	Parameter	Value
Wind sea	Significant wave height [m]	1,20
	Peak period [s]	6,0
Ocean swell	Significant wave height [m]	0,15
	Peak period [s]	15,0
Current	Surface speed [m/s]	0,7

4 Wind buffeting load

Wind simulations are performed in time domain using power spectrum and coherence for the input. Wind time series were generated using Inverse Fast Fourier Transformation (IFFT) algorithm, where frequency dependent wind properties are transformed to time dependent wind fluctuations. The wind fluctuations are applied to the structure as wind buffeting load. All forces on segment section are summed in load vector as aerodynamic wind buffeting forces,

$$F_{wind} = \rho V \begin{bmatrix} C_D & \frac{1}{2}(C_D' - C_L) \\ C_L & \frac{1}{2}(C_L' + C_D) \\ C_M & \frac{1}{2}C_M' \end{bmatrix} \cdot \begin{pmatrix} u \\ w \end{pmatrix} \quad (10)$$

where ρ is wind density, V is wind velocity, C_D, C_l, C_M and C_D', C_L', C_M' are dimensionless drag, lift and moment coefficients and their derivatives on angle of wind attack, u, w are along and vertical wind fluctuations.

4.1 Time fluctuations of wind

The wind field is modelled in time domain with transformation of real spectrum and their coherence to time domain signals. Time signals are correlated with coherence function introducing a correlation between different time series in space. The relation of two correlated nodes M, N in space can according to [6] be written

$$u = \sum_{j=1}^{M} \sum_{k=1}^{N} G_{ij}(\omega) \sqrt{2\Delta\omega} \cos(\omega t + \psi), \qquad (11)$$

where ω is frequency of wind vibration and G_{ij} is correlation matrix at vibration frequency. ψ are independent random phase angles uniformly distributed between 0 and 2π. A very performant IFFT algorithm is used to solve the above equation. Since the correlation matrix is quadratic and symmetrical, a Cholesky decomposition is performed on this matrix of Power Spectrum Densities (PSD),

$$S(\omega) = \begin{bmatrix} S_{11} & \cdots & sim \\ S_{i1} & S_{ij} & \vdots \\ S_{M1} & S_{Mj} & S_{MM} \end{bmatrix}, \qquad (12)$$

where power spectrum for two points in space is calculated as:

$$S_{ij} = \sqrt{S_M S_N} \cdot COH(\omega, \Delta s). \qquad (13)$$

An exponential coherence function,

$$COH = e^{-\frac{\omega}{V}\sqrt{(C_{11}\cdot dx)^2 + (C_{12}\cdot dy)^2 + (C_{12}\cdot dy)^2}} \qquad (14)$$

is used in the present study, where dx, dy, dz are coordinates of distances between two nodes, C_{ij} are the exponential decay factors. $C_{11} = C_{12} = C_{21} = C_{31} = C_{32} = 6{,}5$ and $C_{22} = 3{,}0$ were used.

4.2 Wind field data

Due to uncertainty in the wind conditions at the bridge site, a mean wind speed of $V = 25\, m/s$ across the whole bridge height was chosen as a serviceability limit state. A Kaimal spectrum was used for wind field simulations,

$$PSD = \frac{(TI \cdot V)^2 \, \frac{f}{V} \, L \left(\frac{h}{300}\right)^{eps}}{f\left(1 + 1.5 \, \frac{f}{V} \, L \left(\frac{h}{300}\right)^{eps}\right)^{5/3}}, \qquad (15)$$

where TI is constant turbulence intensity, L is reference length, $eps = 0{,}3$ is an exponential factor, h is height above the ground level. Other wind properties are shown in Table 2.

Table 2. Environmental wind conditions

Environmental load	Load type	Value
Wind (constant wind profile)	Mean wind velocity [m/s]	25,0
Turbulence intensity	Along wind TI_u [%]	12,5
	Horizontal TI_v [%]	9,4
	Vertical TI_w [%]	6,3
Length scale (Kaimal Spectrum)	L_u[m]	700
	L_v [m]	250
	L_w [m]	100

For time simulation time step $dt = 0{,}4$ and simulation time of some 3200 seconds was chosen as a compromise between quality of results and computational effort. The same time scale with frequency band from 0 to 2,5 Hz was used for generating time series, which is a good statistical representation of wind as shown in chapter 4.3.

4.3 Quality of generated wind field

Generated time series can be inspected visually for quality. Input parameters are transformed from frequency domain in to time domain, which are then transformed back to frequency domain, as shown in Figure 8.

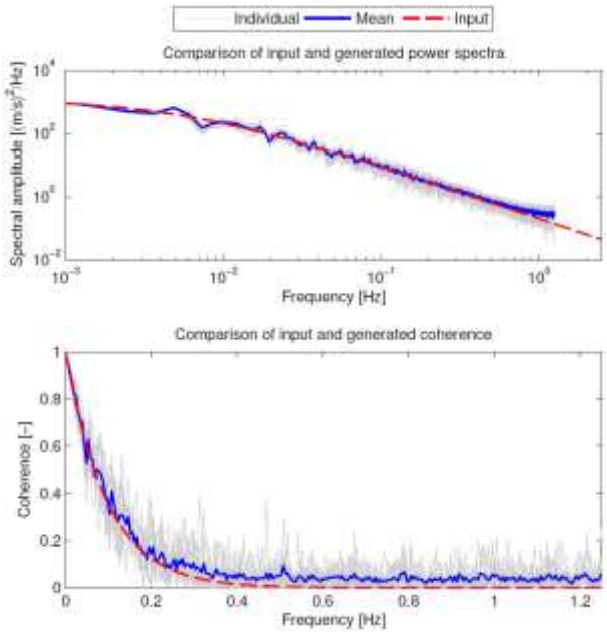

Figure 8. Power spectral density (above) coherence for 40m separation (below) of generated time series. Plots are shown for 13 individual time series (grey), which are averaged out for smoothness (blue). A welch overlapping window function is applied for both power spectra and coherence.

When generating time series in time domain several criteria were checked for quality of generated time series. First a FFT is calculated in generated signal, which should numerically provide similar PSD curve as was used for input. Coherence function introduced to correlation matrix can be checked with auto-correlation calculation of two signals, which is outputted as function of frequency. For better visual presentation overlapping window function were used for performing the FFT transformation, as showed in Figure 8. The FFT results show the accuracy of generated time series. Both input PSD and coherence correspond with the desired properties, as can be observed in Figure 8.

The variance of the signal should be similar for PSD and for generated time series, which is additional verification on transformation quality of the signal. In each wind node both variances are compared and normalised. Small inaccuracy of generated variance can be observed along the deck, as shown in Figure 9. This is an inherent property of the wind field realisation, and can be counter-acted by performing several simulations. The average normalized variance for the along-wind turbulence compoent is 1,014, what is an acceptable discrepancy.

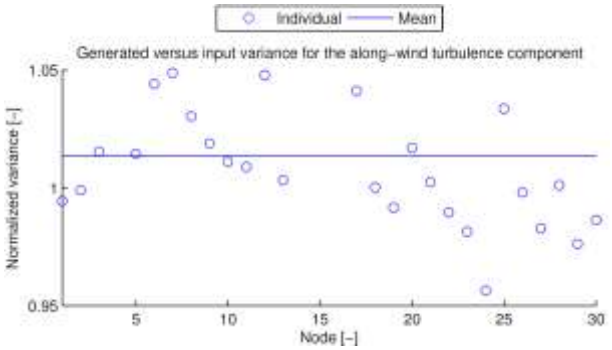

Figure 9. Correlation accuracy of generated time series for nodes along the deck

It has been observed that some average variance factors have a more than 5% deviation in accuracy. If these scenarios are observed more realisations and wind buffeting analyses have to be performed for more accurate results.

5 Results

Simulations were performed for some 3200 seconds, using the same realisation of wind and wave for both concepts. Envelope of motion response is compared in Figure 12, while frequency response spectra of acceleration at selected points along the girder are compared in Figure 13.

The concrete floater exhibits significantly higher displacements, while the maximum accelerations are of similar amplitude. However, both the envelope and response spectra reveal difference in the acceleration response. This is partly due to the large difference in floater inertia, which affects mode frequency and shape, and partly due to floater geometry, which affects wave excitation. Comparing the response spectra of different points along the girder helps reveal how the two concepts respond in the various modes.

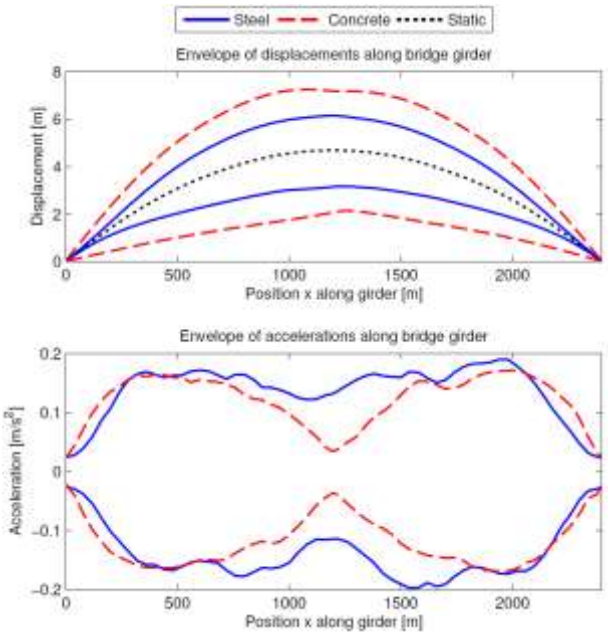

Figure 10. Envelope of displacements (top) and accelerations (bottom). The two concepts have nearly identical static displacement due to mean wind.

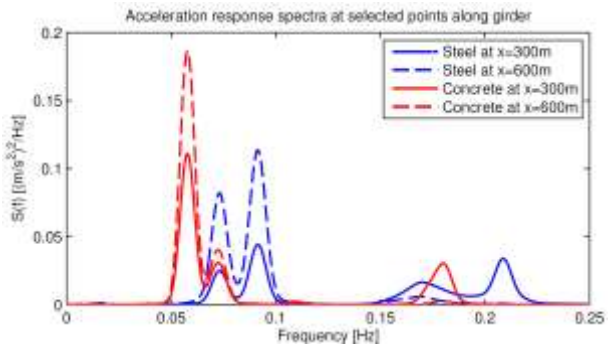

Figure 11. Frequency response spectra of acceleration at quarter span (solid, x=300m) and half span (dashed, x=600m) of the first span. Plots were generated using a parzen window function to resolve the peaks and aid visibility.

6 Conclusion and Future Work

For statistically reliable results many realisations are needed. However the obtained results from a single realisation provide insight into the motion behaviour of the bridge in a severe storm. Displacements and accelerations for both concepts are considered to be within allowable values, but this is for NPRA to decide.

The newly developed functionality in RM Bridge allows us to perform nonlinear time domain analysis of floating bridges with combined wind, wave and current loading. This provides a powerful tool for further development of floating bridge concepts.

Design experience combined with new analysis tools allowing for coupled environmental loading is required to fully understand the behaviour of these amazing bridges.

7 References

[1] Veie J., Holtberget S. Three span floating suspension bridge crossing the Bjørnafjord, proceedings at Multi-Span Large Bridges conference, Porto, 2015.

[2] RM Bridge Advanced, Ver. 10.02., Bentley Systems Austria, 2016

[3] Stampler J., Sello J., Papinutti M., Bruer A., Marley M., Veie J., Helgren Holtberget S., Prediction of Wave and Wind induced Dynamic Response in Time Domain using RM Bridge, Geneva, 2015.

[4] Cummins W. E., The Impulse Response Function and Ship Motions, David Taylor Model Basin, Washington DC, 1962.

[5] ANSYS AQWA Ver. 15.0, ANSYS Incorporated, Canonsburg, PA, 2012.

[6] Strømmen E., Theory of Bridge Aerodynamics, Springer, New York, 2010.